

Electrical modulation and switching of transverse acoustic phononsH. Jeong,¹ Y. D. Jho,^{1,*} S. H. Rhim,² K. J. Yee,³ S. Y. Yoon,¹ J. P. Shim,¹ D. S. Lee,¹
J. W. Ju,⁴ J. H. Baek,⁴ and C. J. Stanton⁵¹*School of Electrical Engineering and Computer Science, Gwangju Institute of Science and Technology,
Gwangju 500-712, Korea*²*Department of Physics and Energy Harvest Storage Research Center, University of Ulsan,
Ulsan 680-749, Korea*³*Department of Physics, Chungnam National University, Daejeon 305-764, Korea*⁴*LED Process Technology Center, KOPTI, Gwangju 500-779, Korea*⁵*Department of Physics, University of Florida, Gainesville, Florida 32611, USA*

(Received 9 June 2015; revised manuscript received 20 April 2016; published 26 July 2016)

We report on the electrical manipulation of coherent acoustic phonon waves in GaN-based nanoscale piezoelectric heterostructures which are strained both from the pseudomorphic growth at the interfaces as well as through external electric fields. In such structures, transverse symmetry within the c plane hinders both the generation and detection of the transverse acoustic (TA) modes, and usually only longitudinal acoustic phonons are generated by ultrafast displacive screening of potential gradients. We show that even for c -GaN, the combined application of lateral and vertical electric fields can not only switch on the normally forbidden TA mode, but they can also modulate the amplitudes and frequencies of both modes. By comparing the transient differential reflectivity spectra in structures with and without an asymmetric potential distribution, the role of the electrical controllability of phonons was demonstrated as changes to the propagation velocities, the optical birefringence, the electrically polarized TA waves, and the geometrically varying optical sensitivities of phonons.

DOI: [10.1103/PhysRevB.94.024307](https://doi.org/10.1103/PhysRevB.94.024307)**I. INTRODUCTION**

Restructuring materials below the acoustic phonon mean-free path or implementing variations in their elastic properties suggested new perspectives regarding the controllability of the acoustic and thermal properties of crystals, such as thermal conductivity management [1,2] and charge transfer via acoustic pulses [3], as well as the concept of phonon lasers [4–7]. Particularly in wurtzite crystals, where pseudomorphic strain caused by lattice mismatch at the interfaces leads to large internal polarization fields, photogenerated carriers screen out the strain-induced piezoelectric field, launching coherent acoustic motions [8–10]. This effect turned out to be very effective compared to thermal strain generation [11] and deformation potential coupling [12]. By virtue of strong electromechanical coupling, acoustic phonons in GaN-based piezoelectric heterostructures have been further investigated in terms of the strain dependence [13], tunability of zone-folded acoustic phonons [14], spatial modulation of acoustic waves [15], and terahertz (THz) electromagnetic radiation at acoustically mismatched interfaces [16,17].

In this regard, GaN-based piezoelectric heterostructures could serve as a versatile test bed for characterizing the acoustic functionalities with extraordinary generation efficiency in the scheme of time-resolved ultrasonics. More specifically, (1) both zone-folded [9,14,15] and propagating phonons [13,18–20] could be detected; (2) because of the small absorption depth (≤ 100 nm) compared to the conventional excitation spot size (≥ 10 μm), the mode of the generated phonons depends on the growth direction; e.g., transverse acoustic (TA) and longitudinal acoustic (LA) phonons can appear

simultaneously in the anisotropic plane [19,20], or LA phonons alone can be generated in the isotropic c plane [13,15,18]; (3) both the deformation potential and displacive screening of electric fields, combined with the piezoelectricity, contribute to generating acoustic phonons having compositional amplitudes that depend on the crystal axis [8].

Owing to the well-established crystallinity of wurtzite semiconductors along the symmetry axis, where no shear mode can be excited by photoexcitation, and their poor detection sensitivity for TA phonons [21], previous studies were rather restricted to the LA properties among the three polarizations. On the other hand, the TA modes have been of great interest in the analysis of physical properties, such as shear viscosity in liquids [22–25] or elasticity and/or photoelasticity in solids [20,26–32], and can provide nanoscale diagnostics [33] with twice the temporal resolution because of their slow propagation velocities (approximately half that of the LA mode).

To exploit the shear acoustic properties, several experimental techniques under pulsed laser excitations have been developed based on (1) the LA-to-TA mode conversion [21,27,34–37] and (2) the direct activation of TA mode in anisotropic crystals [20,28–32]. The mode conversions were achieved via tight focusing of pump beams on an isotropic metal film within a spot size of $1 \sim 2$ μm to reduce the acoustic directivity along the surface normal [34,35], the transient interference patterns of two pumping beams on molecular solids [27], and reflections of LA modes at isotropic-anisotropic crystal interfaces [21,37]. However, it could be practically advantageous to generate and control TA mode in those schemes for inspecting nanostructures or characterizing material parameters with well-aligned propagations along the depth direction as well as better intermode conversion efficiency. In this regard, the direct excitation mechanisms have been proposed in materials

*jho@gist.ac.kr

with broken symmetry to improve the directivity and excitation efficiency: anisotropic thermoelastic expansions in asymmetrically cut metals [28,32], Raman scattering in low-symmetry superlattices [30], and symmetry-dependent piezoelectric and deformation potential couplings in anisotropic ferroelectric oxides [29] and semiconductors [8,19,20], such as *a*-plane wurtzite GaN. In most previous efforts, however, the growth direction was considered to be the crucial factor determining the axial symmetry and concomitant strength of the acoustic phonon modes generated.

From the viewpoint of prospective device applications, it would be useful if an external bias could play a role in modifying the characteristics for generating and detecting acoustic phonons. For example, under an external reverse bias in GaN-based piezoelectric diodes, the amplitude of the LA mode propagating along the *c* axis [18] and the localized TA mode along the non-*c* axis were independently enhanced [19]. We demonstrated a switching scheme of TA phonons in a laterally biased piezoelectric diode [33], where the amplitude and switching time of the TA mode could be electrically modulated.

In this work, we experimentally examine the relative roles of the electric potential distributions in selection rules for acoustic mode generation and detection. For comparison, the acoustic phonon properties were measured from samples with or without an asymmetric potential distribution by utilizing an ultrafast optical pump-probe scheme and terahertz time-domain spectroscopy (THz-TDS). The structure with the asymmetric potential gradients further revealed frequency shifts of the observed phonon signals due to modulation of the elasticity.

The paper is organized as follows. We introduce the growth parameters, band structures, and strain-induced structural distortions of two contrasting samples, one under an asymmetrical potential distribution and the other under a symmetrical potential distribution, in Sec. II. Our experimental schemes are briefly described in Sec. III. In Sec. IV, we present the experimental results for electrical manipulation of the acoustic mode generations. In Sec. V, the role of lateral electric field in modal detection is discussed in terms of the birefringence and detection sensitivity modulation under different potential distributions. Finally, we summarize our findings and conclusions in Sec. VI.

II. SAMPLES WITH DIFFERENT ELECTRIC POTENTIAL DISTRIBUTIONS

Figures 1(a) and 1(b) show micrographs of two representative structures with distinct potential distributions. They have similar vertical structures with multiple quantum wells (QWs) placed within the intrinsic region of *p-i-n* diodes grown along the *c* axis, where the reverse applied bias compensates for the piezoelectric field [38]; the fundamental difference between them lies in the symmetry of the potential distributions. The sample under an asymmetric potential distribution (sample A hereafter), shown in Fig. 1(a), has a so-called interdigitated structure with narrow *p* and *n* electrodes that are laterally spaced by $\sim 100 \mu\text{m}$ along the *x* direction on top of a thin indium tin oxide (ITO) layer ($\sim 40 \text{ nm}$). In this way, an electric current *I* along the *x* axis was unevenly applied in sample A. In contrast, the contact electrodes of the sample

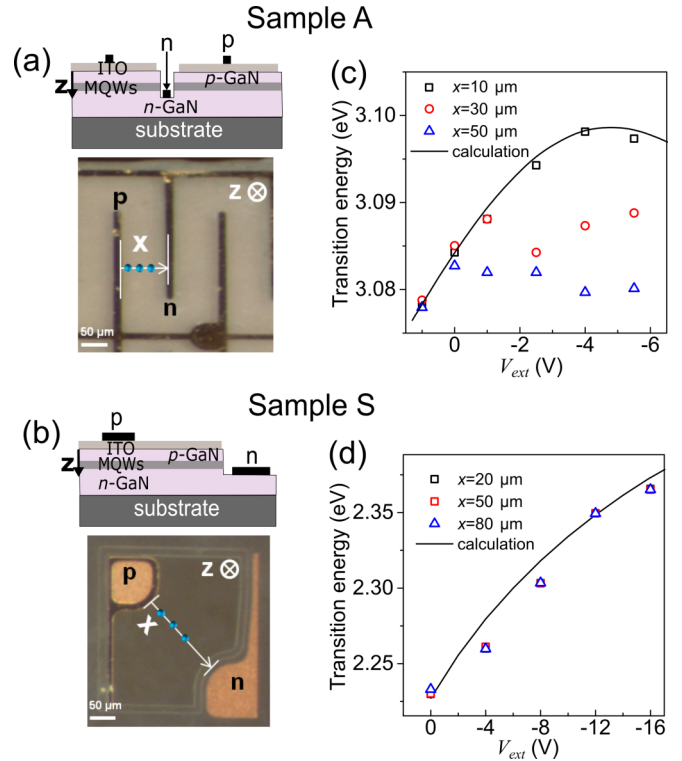


FIG. 1. Side and top views of (a) sample A and (b) sample S, where the blue dots along the *x* axis from the *p* contact to the *n* contact denote the laser excitation spots for the PL measurements. PL peak energy as a function of external bias in (c) sample A and (d) sample S.

under a symmetric potential distribution (sample S hereafter), shown in Fig. 1(b), were much wider, with a thicker ITO layer ($\geq 150 \text{ nm}$) to evenly spread *I* in the *x-y* plane. The following layers were sequentially grown on sapphire substrates by metal-organic chemical vapor deposition in sample A (sample S): 3- ($0.5-$) μm -thick undoped GaN, 2.5- ($3-$) μm -thick *n*-GaN, six (five) QW layers of 2-nm-thick $\text{In}_{0.1}\text{Ga}_{0.9}\text{N}$ (1.5-nm-thick $\text{In}_{0.25}\text{Ga}_{0.75}\text{N}$) encased by seven (six) 8- ($7.5-$) nm-thick GaN barriers, 120- ($70-$) nm-thick $p\text{-Al}_{0.05}\text{Ga}_{0.95}\text{N}$ ($p\text{-Al}_{0.15}\text{Ga}_{0.85}\text{N}$), and 250- ($140-$) nm-thick *p*-GaN. The electron and hole concentrations in sample A (sample S) were estimated to be about 7×10^{17} (2×10^{17}) cm^{-3} and 8×10^{17} cm^{-3} , respectively.

Figures 1(c) and 1(d) show the results of spatially resolved photoluminescence (PL) measurements, where a frequency-doubled Ti:sapphire laser was used as an excitation source at 367.5 nm with a spot size of $\sim 10 \mu\text{m}$. The emission properties of the samples differed greatly. As the excitation spot moved away from the *p* electrodes, the PL peak energy was red-shifted under the external bias V_{ext} only in sample A. In the conventional case of sample S with an even current distribution, on the other hand, no notable energy shift was observed with *x*, as expected. The PL energy shift is well understood in terms of the quantum-confined stark effect [39]. A typical PL peak for spontaneous emission should be matched with the lowest-lying QW transition and determined on the basis of the net electric field in the QW, E_z^w . Hence, the red-shift of the PL peak energy with *x* in sample A intuitively

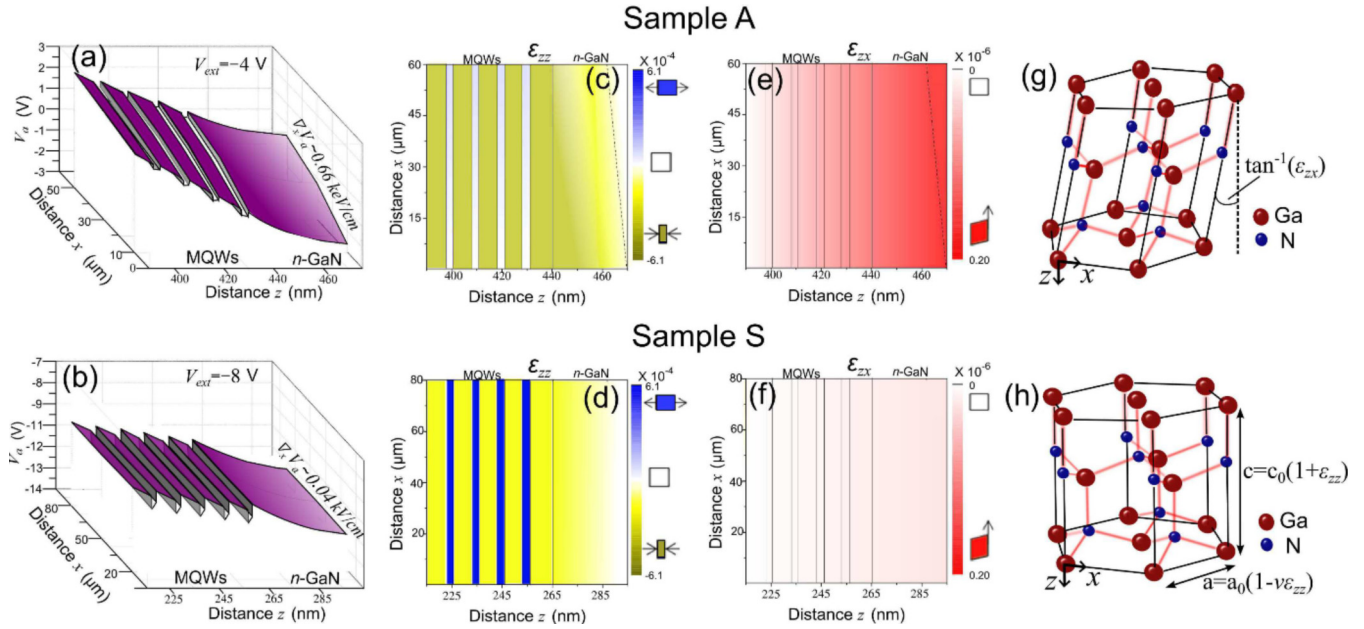


FIG. 2. Electric potential profiles of (a) sample A and (b) sample S near MQWs/*n*-GaN interface. Distributions of normal strain ε_{zz} in (c) sample A and (d) sample S. Shear strain ε_{zx} distributions in (e) sample A and (f) sample S. Distortions in the lattice structures of (g) sample A and (h) sample S.

indicates that the actual magnitude of the vertically applied voltage decreased along x . To determine the energy band profiles in the x - z plane, E_z^w was extracted from the variational calculations of the PL peak energy. As E_z^w and the net electric field in the barrier E_z^b were formulated using the built-in potential V_{bi} , the vertically applied voltage V_a could be subsequently evaluated as a function of x and z . The piezoelectric field E_F was set to 0.98 MV/cm in sample A and 3.7 MV/cm in sample S, as indicated by the solid lines in Figs. 1(c) and 1(d).

The resultant electric potential profiles, incorporating the exerted potential distributions of $V_a(x, z)$, are shown in Figs. 2(a) and 2(b) for sample A at -4 V and sample S at -8 V, respectively. Following the procedures introduced above, the magnitude of E_z^b (~ 0.8 MV/cm in sample A and ~ 0.5 MV/cm in sample S) reproduced the rapid potential variations along the z direction in both samples. Further, the PL energy variations in Fig. 1(c) ultimately substantiated the increasing lateral electric field $E_x = -\nabla_x V_a$ in sample A, reaching ~ 0.66 kV/cm at -4 V at the end of the depletion region. The magnitude of E_x at -4 V was similar to that of E_z^w in sample A but negligible in sample S. Accordingly, the tensor components of the mechanical strain are subjected to distinct potential profiles in the piezoelectric structures exposed to the external bias. In particular, the additive lateral electric field E_x in sample A could induce shear strain, which is otherwise forbidden.

According to the piezoelectric matrix, the strain components are connected by the electric field distributions:

$$\begin{bmatrix} \varepsilon_{xx} \\ \varepsilon_{yy} \\ \varepsilon_{zz} \\ \varepsilon_{yz} \\ \varepsilon_{zx} \\ \varepsilon_{xy} \end{bmatrix} = \begin{bmatrix} 0 & 0 & d_{31} \\ 0 & 0 & d_{32} \\ 0 & 0 & d_{33} \\ 0 & d_{24} & 0 \\ d_{15} & 0 & 0 \\ 0 & 0 & 0 \end{bmatrix} \begin{bmatrix} E_x \\ E_y \\ E_z \end{bmatrix}, \quad (1)$$

where the piezoelectric strain constants are $d_{31} = d_{32} = -1.9$ pmV $^{-1}$, $d_{33} = 3.7$ pmV $^{-1}$, and $d_{15} = d_{24} = -3.1$ pmV $^{-1}$ according to the previously published data for wurtzite GaN with 6-mm symmetry [40]. Then, the normal (ε_{zz}) and shear strain components (ε_{zx}) in the x - z plane were calculated from the results in Fig. 1(c) [Fig. 1(d)] at -4 V for sample A (at -8 V for sample S) and are spatially mapped in Figs. 2(c)–2(f), respectively. The signs of the normal strains (ε_{zz}) in Figs. 2(c) and 2(d) are opposite to those of the in-plane strains (ε_{xx} and ε_{yy}), revealing positive Poisson ratios; the normal strains were compressive in the barriers and tensile in the QWs. On the other hand, the shear component (ε_{zx}) of sample A, shown in Fig. 2(e), became prominent throughout the biased region and was maximized near the end of the n -depletion region, in contrast to the suppressed values in sample S, shown in Fig. 2(f), due to the absence of the lateral electric field. The strain-induced structural distortions are illustrated schematically in Figs. 2(g) and 2(h). The volumetric deformation in Fig. 2(h) for sample S, where the lattice constants are modified to $c = c_0(1 + \varepsilon_{zz})$ and $a = a_0(1 - \nu\varepsilon_{zz})$ from the strain-free values of c_0 and a_0 , implies that the structure is still laterally isotropic under an external bias V_{ext} . In contrast, in sample A under a shear strain ε_{zx} , monoclinic distortion that is geometrically defined by an angle θ to tilt the c axis [41] breaks the optical and mechanical symmetry in the c plane in Fig. 2(g).

III. EXPERIMENTAL SCHEMES FOR MEASURING PHONON DYNAMICS

Time-resolved pump-probe measurement and THz-TDS were conducted for various values of V_{ext} or the angular parameters (θ, ϕ) to identify the role of the electric potential distributions in affecting both the detection and generation of acoustic phonons. A pair of Ti:sapphire lasers, synchronized

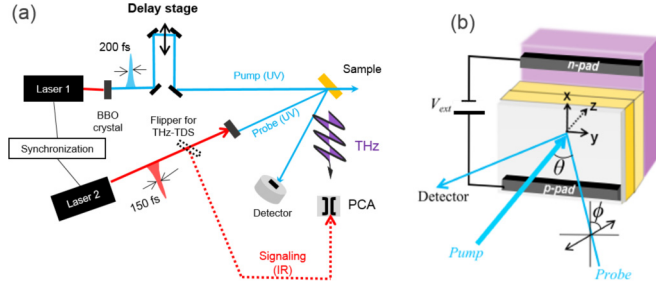


FIG. 3. (a) Experimental scheme for time-resolved pump-probe and THz measurements using frequency-doubled Ti:sapphire lasers. (b) Illustration of measurement geometry for probing acoustic modal dynamics.

at 76 MHz and with a jitter (~ 113 fs) smaller than the pulse width (~ 250 fs), was used at either 367.5 nm (for THz-TDS) or 367.5–375 nm (for pump-probe measurement) in the reflective geometry, as shown in Fig. 3(a). For THz-TDS, each laser could be used as either a pumping source for THz generation or a signaling source (fixed at 800 nm) for detection via a Si lens coupled with a photoconductive antenna; the laser wavelengths were degenerate for pump-probe measurement. The fluence of the pump beam for both pump-probe measurement and THz-TDS was $\sim 85 \mu\text{J}/\text{cm}^2$, and the ratio to that of the probe beam was 8:1. The laser spot size was maintained within $\sim 20 \mu\text{m}$ for the measurements. The angular parameters of the measurements are further illustrated in Fig. 3(b). The incident angle θ of the pump beam from the surface normal was fixed at 45° (for THz-TDS) or zero (for pump-probe measurement), whereas the θ value of the probe beam was set to less than 5° unless otherwise mentioned (cf. Figs. 8 and 9).

IV. ROLE OF LATERAL ELECTRIC FIELD IN ACOUSTIC PHONON GENERATION

In this section, we show that the application of an external bias in the c plane can break the selection rules of isotropic c -GaN, switching on the normally forbidden TA mode. To explicitly show the differing roles of vertical and lateral electric fields in the generation process, a strain-dependent model of the acoustic wave equation was developed. Our experimental results further demonstrate that the modal propagation velocities are controllable under an external bias. In addition, the switching time of the TA mode can be effectively manipulated by changing the scale of the laterally biased region.

A. Electrically controlled acoustic mode generations

When coherent acoustic phonons are displacively initiated via the transient electric field screening by the photocarriers, the relevant dynamic features can be described on the basis of a typical loaded-string equation [8]

$$\frac{\partial^2 u_i}{\partial t^2} - v_i^2 \frac{\partial^2 u_i}{\partial z^2} = \frac{1}{\rho_0} S_i(x, z, t), \quad (2)$$

where i stands for each phonon mode (LA or TA), u_i represents the atomic displacement, ρ_0 is the mass density, and v_i is the

modal velocity. The driving force $S_i(x, z)$ is quantified as

$$\begin{bmatrix} S_{xx} \\ S_{yy} \\ S_{zz} \\ S_{zy} \\ S_{zx} \\ S_{xy} \end{bmatrix} = \begin{bmatrix} \Delta\sigma_{xx} \\ \Delta\sigma_{yy} \\ \Delta\sigma_{zz} \\ \Delta\sigma_{zy} \\ \Delta\sigma_{zx} \\ \Delta\sigma_{xy} \end{bmatrix} = \begin{bmatrix} 0 & 0 & e_{31} \\ 0 & 0 & e_{31} \\ 0 & 0 & e_{33} \\ 0 & e_{24} & 0 \\ e_{15} & 0 & 0 \\ 0 & 0 & 0 \end{bmatrix} \begin{bmatrix} \Delta E_x \\ \Delta E_y \\ \Delta E_z \end{bmatrix}, \quad (3)$$

where $\Delta\sigma$ is the instantaneous stress change, e_{ij} is the piezoelectric stress constant, and ΔE_j is the screened electric field intensity along the direction j . In this model, S_{LA} ($= S_{zz}$) is simplified by $(2\frac{d_{31}}{d_{33}}C_{13}^0 + C_{33}^0)\Delta\epsilon_{zz}$, where $\frac{d_{31}}{d_{33}} \sim -0.5$ represents the Poisson effect, and S_{TA} ($= S_{zx}$) is $C_{44}^0\Delta\epsilon_{zx}$. By assuming complete field screenings in the epicenters under the instantaneous laser excitation, the general form of driving force is

$$S_i(x, z, t) = \bar{C}_i \epsilon_i(x, z) H(t), \quad (4)$$

where the roles of the externally applied strains and photocarriers are clearly distinguished. The selection of the acoustic mode is determined by the strains ϵ_{LA} (ϵ_{zz}) and ϵ_{TA} (ϵ_{zx}), with the corresponding effective modal constants $\bar{C}_{LA} = 2\frac{d_{31}}{d_{33}}C_{13}^0 + C_{33}^0$ and $\bar{C}_{TA} = C_{44}^0$, respectively. The extra term $2\frac{d_{31}}{d_{33}}C_{13}^0$ in \bar{C}_{LA} resulted from the contribution of the in-plane strain changes ($\Delta\epsilon_{xx}$ and $\Delta\epsilon_{yy}$) to the normal stress change $\Delta\sigma_{zz}$. The instantaneous initiation of each mode by abrupt field screening is described by the Heaviside step function $H(t)$ without regard to the mode index i . In this description, only the piezoelectric effect was considered because of its dominant role in the generation process in samples grown along the c axis [8].

Ultrafast modification of the potential profiles by photocarriers initiates the propagating acoustic waves; the probe laser waves encounter the modal acoustic waves at different positions and are partially reflected by or transmitted through the wave packets [13,42]. Considering the dynamic Fabry-Perot interference between the reflection from the surface $r_0 = \frac{1-n}{1+n}$ and the reflection from an acoustic wave packet $\eta_i(z, t)$, $\Delta R/R \propto \frac{\partial n}{\partial \eta_i} \eta_i(z, t)$, the differential reflectivity change $\Delta R/R$ is simply expressed as $\int dz F_i \cos(2nkz + \phi_F) \eta_i(z, t)$ [42], where n is the refractive index, F_i is the detection sensitivity of $\eta_i(z, t)$ in a medium, k is the wave number of the probe light, and ϕ_F is a phase angle. Consequently, the oscillation frequency components of $\Delta R/R$ are expressed as $f_i = 2v_i n \cos(\theta_i) / \lambda_{\text{probe}}$, where θ_i is the angle of the probe transmission inside the materials and λ_{probe} is the wavelength of the probe beam.

The transient oscillations in reflective pump-probe measurements under V_{ext} have accordingly been extracted from $\Delta R/R$ based on the sliding-window fast Fourier transform spectra, as shown in Figs. 4(a) and 4(b). In sample A, not only f_{LA} at 119 GHz but also the novel spectral component at 70 GHz emerged under an external bias V_{ext} . f_{LA} matches well the v_{LA} value of ~ 7300 m/s; this was further confirmed by the time of flight, which was revealed by an abrupt phase jump at the GaN-sapphire interface [13], whereas the lower-frequency component (70 GHz) was ascribed to a new acoustic mode with v_{TA} (~ 4200 m/s [43]), generally forbidden in isotropic structures. To verify that the 70-GHz component from sample

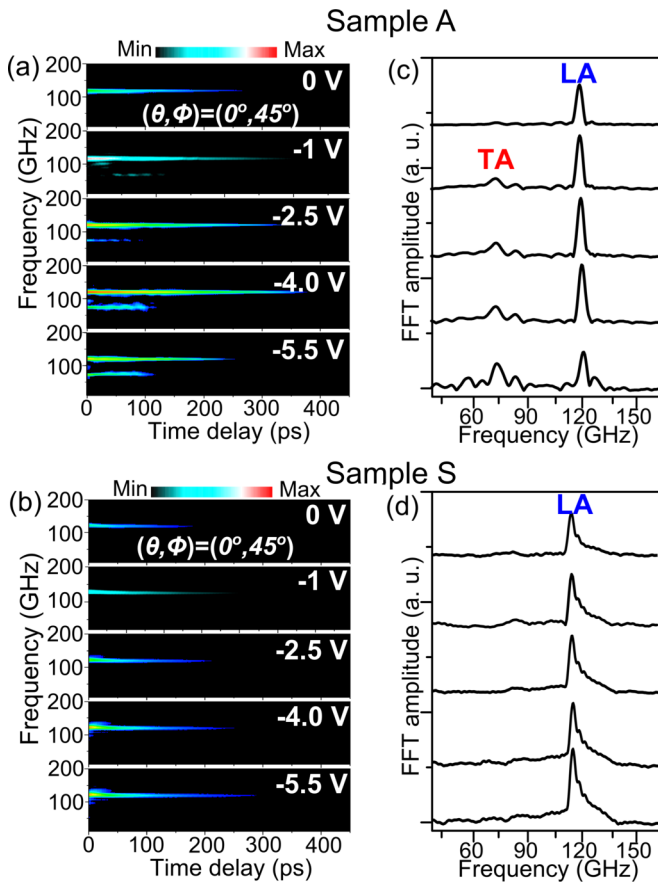


FIG. 4. Sliding-window fast Fourier transform spectra of the dynamic Fabry-Perot interference from (a) sample A and (b) sample S under reverse bias from 0 to -5.5 V. The contour plots show spectral information (vertical axis) with respect to the time delay (horizontal axis). Integrated spectra over the entire temporal range for (c) sample A and (d) sample S.

A originated from the TA mode, the prominent frequencies measured with various values of λ_{probe} were converted into the corresponding velocities [33]. In clear contrast, sample S without lateral fields showed a monochromatic spectral component of the amplitude of which increased gradually with the reverse external bias from 0 to -5.5 V.

In terms of the modal amplitudes, the bias-dependent changes in sample A were further explained by the different distributions of the normal and shear strains in Figs. 2(c) and 2(e), respectively. The strength of the screening electric field and the width of the epicenters can be estimated using a simple virtual capacitor model [44] formed of the accumulated photocarrier distributions. For coherent LA phonon generation, electric fields transiently induced by photocarriers within multiple QWs (referred to as in-well screening [18]) play a major role. As V_{ext} increases, however, the reduced effective barrier widths result in considerable electronic tunneling, together with thermionic emission of holes over the lower valence band barriers [39]. In this way, the charge densities of the serially connected virtual capacitors within the multiple QWs decrease; thus, the contribution of the QW carriers to acoustic mode generation also decreases. Therefore, the

suppressed LA mode signal after -4 V in Figs. 4(a) and 4(c) implies that LA phonons originate from the QWs.

At a large external bias V_{ext} , the macroscopic screening, the spatial extent of which encompasses the intrinsic and depletion regions (referred to as out-of-well screening [45]) may possibly become as important as the in-well screening. Under these conditions, the photocarrier sweep-out under the vertical electric field (~ 0.8 MV/cm at -4 V) leads to virtual capacitor formation, where the relevant sheet carrier densities are obtained by integrating the photocarrier distributions over the screening distance. Using the photocarrier density observed under a pump fluence of $80 \mu\text{J}/\text{cm}^2$ and the high-frequency dielectric constant [46], the required screening distance to compensate for the electric field of ~ 0.8 MV/cm was estimated to be ~ 40 nm. Because of the significant saturation velocity difference between electrons and holes in GaN (a factor of ~ 12 [47,48]), the photoexcited electrons immediately accumulate at the boundary of the n -depletion region within ~ 0.4 ps, whereas the much slower holes take more than 5 ps to cross the entire macroscopic region. Therefore, during the acoustic mode generation period (~ 0.5 ps), a virtual capacitor scaled around 40 nm [44] could be spatially formed near the n -depletion region where shear strains are prominent, as shown in Fig. 2(e). In this regard, the TA signal, whose amplitude persistently grows with V_{ext} despite QW tunneling, is thought to be generated mostly from the n -depletion region.

B. Mode-dependent temporal line-shape analysis

The propagation directions and spatial origins of the acoustic modes can be explicitly identified by tracing the amplitudes and phase changes of the oscillatory components of $\Delta R/R$. To explore different modal behaviors in sample A, the oscillatory signal (black line) at -4 V was band-pass filtered at around the TA and LA modes (yellow scattered lines), as shown in Fig. 5(a). Because of the limited skin depth ξ of the probe beam (~ 700 nm), the envelope for a descending acoustic wave packet (η_i^d , where i indicates the phonon mode, LA or TA) would decay with time, whereas the envelope for an ascending wave packet (η_i^a) grows as η_i^a approaches the surface [15]. The amplitude change of each mode before the propagation time in the anisotropic region τ_i in Fig. 5(a) could be fitted by considering both η_i^a and η_i^d components (red and blue lines).

When the values of τ_i are multiplied by the corresponding velocities, they are converted into the propagation distances of the acoustic phonons ascending from the epicenters to the surface (and vice versa for η_i^d). The distance for the LA mode (~ 415 nm) coincides well with the distance from the center of the intrinsic region to the surface (405 nm). Therefore, η_{LA}^a is considered to be generated mainly from the MQWs, as in conventional cases [13,42]. In contrast, the TA mode traveled ~ 80 nm farther than the LA mode, which is approximately the sum of half the intrinsic region and n -depletion region widths $l_D(n_e, n_p, V_{\text{ext}})$ [39]. Thus, η_{TA}^a was considered to be launched mainly from the n -GaN depletion region, as can be further inferred from the shear strain distribution, maximized near the n -depletion region in Fig. 2(e). For this reason, the slightly increased value of τ_{TA} between -1 and -5.5 V (~ 20 ps) could be converted into the enlarged travel distance of 84 nm in accordance with the expanded depletion region width at the

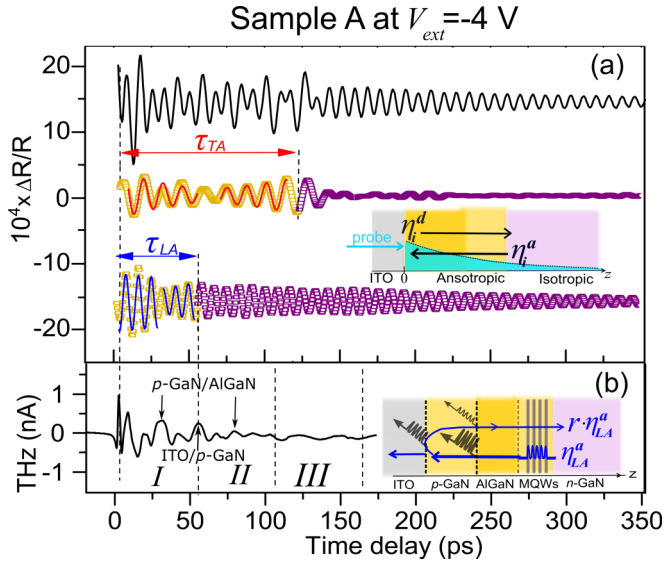


FIG. 5. (a) Total oscillatory component in pump-probe signal (black line) was filtered into the TA (52–88 GHz) and LA mode (108–144 GHz) frequencies. Inset illustrates the spatial origins and propagations of the acoustic modes. (b) THz radiation as a function of time delay. Inset correlates the THz signal with the propagation of the ascending LA wave packet.

surface and in the n -GaN region. This agreement between the transient digitized appearance and the travel path of the TA mode in Fig. 5(a) also confirmed that TA modes can be not only generated, but also detected only in the laterally biased anisotropic region.

The initial deviations of the acoustic modes from the fitting curves are attributed to partial propagation of the surface-generated strain components toward the surface [11] considering the relatively wide surface depletion region (~ 150 nm) [49]. Without an ITO layer, the reflection of an acoustic mode from the air/ p -GaN interface would be almost 100% [11,15] without diffuse phonon scattering. In our case, however, the acoustic mode reflection from the ITO/ p -GaN interface is estimated to be ~ 0.25 (0.19) for the LA (TA) mode, on the basis of the acoustic impedance mismatch between GaN [50] and ITO [51].

The acoustic reflectivity at the p -GaN/ITO interface r together with the spatial origins were investigated by measuring the emitted THz waves during phonon propagations in Fig. 5(b). When an acoustic wave packet η_i traverses a piezoelectric interface, transient polarization currents are induced as $j_i^{\text{int}} \propto -(1/d_{1,i} - 1/d_{2,i})v_i\eta_i(z_{\text{int}} - v_it)$, where $d_{1,i}$ and $d_{2,i}$ are the piezoelectric strain constants of the adjacent layers for mode i , as previously reported for LA waves [16,17]. Therefore, the transient THz emission patterns directly indicate the acoustic wave profiles crossing the interfaces at the position of z_{int} as illustrated in the inset of Fig. 5(b); e.g., the temporal width of a THz pulse coincides with the spatial width of η_i divided by v_i .

By comparing the mode-dependent transient pump-probe spectra in Fig. 5(a) to the THz line shapes in Fig. 5(b), only the LA waves are coupled to the carriers with the piezoelectric polarization aligned along the direction of propagation, which

induces the THz radiations. To reduce complexity in the analysis, we focused on the propagation of the most intense strain component η_{LA}^a , dividing the THz signal into three temporal domains. In time domain I ($0 < t < \tau_i$), η_{LA}^a travels from the multiple QWs toward the ITO/ p -GaN interface. The fast signal at the beginning is probably explained by surge photocurrent generation in the sample [52]. The signal at $t \sim \tau_{\text{LA}} - 25$ ps (denoted by arrow) is attributed to the interaction between η_{LA}^a and the p -GaN/AlGaN interface. In time domain II ($\tau_i < t < 2\tau_i$), the acoustic packet is reflected from the ITO/ p -GaN interface with a reduced amplitude of $r \cdot \eta_{\text{LA}}^a$. The amplitude ratio ($\sim 30\%$) of the signals at $t \sim \tau_{\text{LA}} \pm 25$ ps (denoted by arrows) was in good agreement with the reflection of $\sim 25\%$ estimated from the acoustic impedance mismatch. The lingering slow oscillations in time domain III ($2\tau_i < t < 3\tau_i$) are suspected to be generated by acoustic phonon-carrier interactions in the n -GaN side.

C. Electric-field-induced propagation velocity modulation

Another intriguing feature of the electrically controlled acoustic mode dynamics is the spectral blue-shifts of f_i in both samples under increasing V_{ext} in Figs. 4(c) and 4(d). To investigate the external-field-dependent dynamic properties of the acoustic modes using the information $f_i \propto v_i n$, we first traced the refractive index changes with V_{ext} by measuring the ellipsometric parameters [33]. On the other hand, the modal spectra of the dynamic Fabry-Perot oscillations were traced without phase-change-induced errors by selecting temporal ranges for the FFT between $\tau_i/2$ and τ_i , as shown in Figs. 6(a) and 6(b) for samples A and S, respectively. The peak frequencies of both the LA and TA modes in sample A increased by $\sim 1.7\%$ with increasing V_{ext} in Fig. 6(c). In contrast, the spectral shift of the LA mode in sample S in Fig. 6(d) was relatively negligible, $\sim 0.25\%$. Then, inserting

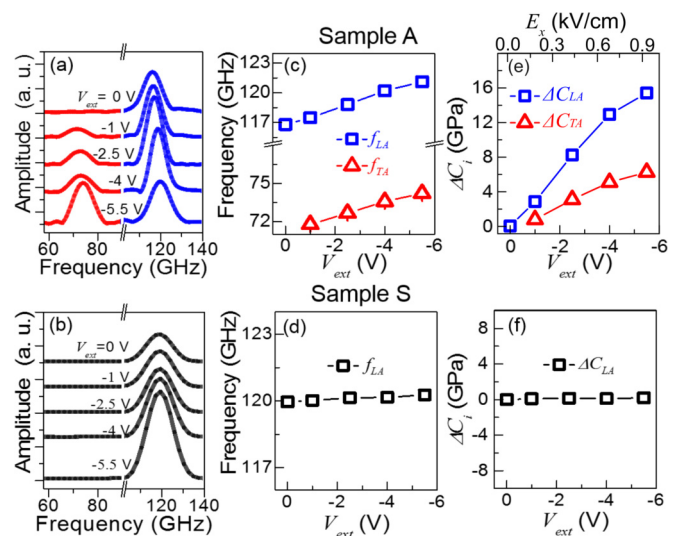


FIG. 6. FFT spectra for the ascending waves in (a) sample A and (b) sample S as a function of V_{ext} . Spectral peak frequencies of acoustic modes in (c) sample A and (d) sample S under different V_{ext} . V_{ext} -induced elastic constant variations in (e) sample A and (f) sample S.

the separately measured n into f_i under V_{ext} , we extracted v_i equal to $\sqrt{\frac{C_i^0 + \Delta C_i(V_{\text{ext}})}{\rho_0}}$ and $\Delta C_i(V_{\text{ext}})$ in Figs. 6(e) and 6(f).

Here, the origins of modal velocity modulation in wurtzite semiconductors could be inspected in terms of the following mechanisms: (1) deviation of the acoustic mode propagation direction out of the symmetry axis [8,53], (2) strain-induced perturbations on elastic constants [33], and (3) carrier-phonon interactions [54,55]. Since, in our experimental scheme, the behavior of the photogenerated acoustic waves was ensured to be one dimensional along the surface normal with a deviation angle smaller than 10^{-6} degree from the symmetry axis, the effect of the propagation direction change could be safely ignored in extracting ΔC_i .

Instead, we examined the combined influence of the structural distortions, volumetric deformations by E_z , and tilting of the symmetry axis by E_x , on acoustic phonon velocities in the context of the elastic tensor perturbations (cf. Appendix A for matrix representations). In this way, the bias-dependent changes $\Delta C_i(V_{\text{ext}})$ in Figs. 6(e) and 6(f) could be compared with the perturbation-based analytical expressions: $\Delta C_{\text{LA}}^{\text{pert}} \simeq C_{333}^H d_{33} E_z + \frac{(C_{355}^M)^2}{C_{33}^0 - C_{44}^0} d_{15}^2 E_x^2$ and $\Delta C_{\text{TA}}^{\text{pert}} \simeq C_{443}^H d_{33} E_z - \frac{(C_{355}^M)^2}{C_{33}^0 - C_{44}^0} d_{15}^2 E_x^2$, where ϵ is the dielectric constant and C_{lmn}^H (C_{lmn}^M) is the third-order elastic (TOE) constant, coupled with E_z (E_x). The relatively moderate behavior of f_{LA} with V_{ext} in sample S implies that E_z hardly affects C_i of wurtzite GaN within the range of V_{ext} for both samples. Ignoring the influence of E_z , the expression ΔC_i^{pert} could be simplified in terms of E_x as $\Delta C_{\text{LA}}^{\text{pert}} \simeq \frac{(C_{355}^M)^2}{C_{33}^0 - C_{44}^0} d_{15}^2 E_x^2$, and $\Delta C_{\text{TA}}^{\text{pert}} \simeq -\frac{(C_{355}^M)^2}{C_{33}^0 - C_{44}^0} d_{15}^2 E_x^2$. The dominant role of E_x in modifying elastic constants is substantiated in Fig. 6(e) in comparison with the experimental results from sample S.

However, we cannot theoretically quantify the amount of velocity change since the TOE tensor components are yet to be quantified in the GaN-based materials. The abnormal changes in the acoustic frequencies under the combined distortion by the normal and shear strains possibly indicate that the atomic restoring force is nonlinear in displacement. Intuitively, such behaviors could be attributed to the distorted electron cloud of the atomic system in a way that the harmonic constants of the interatomic potential were drastically modified by broken optical and mechanical symmetry. Even so, the increasing behavior of ΔC_{TA} in Fig. 6(e), which could not be quantified by the perturbation-based model, implies that the influence of E_x on phonon velocities could not be described solely by the structural distortions.

In order to understand the elastic constant modifications more quantitatively, the interactions between acoustic phonon modes and free carriers, which have been neglected so far, should be incorporated into the perturbation-based model. In piezoelectric materials without free carriers, the elastic constant C_i for each acoustic mode remains stiffened [53] by $\Delta C_i^{\text{stif}} = \frac{e_i^2}{\epsilon}$, compared to the opposite extreme case of heavily doped materials. For wurtzite GaN, the stiffening is estimated to be ~ 5.5 GPa (~ 1.2 GPa) for LA (TA) mode based on the previously reported value of the piezoelectric constant [56] $e_{\text{LA}} = e_{33} = 0.65$ C/m² ($e_{\text{TA}} = e_{15} = -0.3$ C/m²). In the presence of intermediate free-carrier density N , the stiffening

of elasticity can be modulated via screening of the piezoelectric field [54] as $\Delta C_i^{\text{stif}} = \frac{e_i^2}{\epsilon} \frac{1}{1 + (Nq\mu/\epsilon\omega_i)^2}$, where q is the electronic charge, μ is the mobility, and ω_i is the central frequency of acoustic phonon packet. The critical density N_c ($= \frac{\epsilon\omega_i}{q\mu}$), where the halfway point occurs, was estimated to be $\sim 1 \times 10^{17}$ cm⁻³ ($\sim 1.2 \times 10^{16}$ cm⁻³) in p -GaN and $\sim 2 \times 10^{16}$ cm⁻³ ($\sim 2.7 \times 10^{15}$ cm⁻³) in n -GaN for LA (TA) mode. In this regard, at low densities ($N < 0.1N_c$), the total change ΔC_i ($= \Delta C_i^{\text{stif}} + \Delta C_i^{\text{pert}}$) can be expressed as $\frac{e_i^2}{\epsilon} + \Delta C_i^{\text{pert}}$; whereas, $\Delta C_i \simeq 0$ at high densities ($N > 10N_c$) because ΔC_i^{stif} , which is based on piezoelectricity, is also screened out by sufficiently large number of carriers.

In the temporal range of $\tau_i/2 < t < \tau_i$, over which the FFT spectra were obtained in Fig. 6, the ascending mode propagating in the p -GaN regions dominated the signals. Accordingly, in sample A, the E_x over the entire anisotropic region, which was indicated by the digitized appearance of TA mode in Fig. 5(a), could reduce the carrier density through the lateral transport of holes regardless of E_z , increasing C_i . Although the E_x -dependent hole density variation could not be explicitly quantified in sample A under the current scheme, it was confirmed from a separate measurement under lateral p - i - n structure that the lateral field intensity of 0.5 kV/cm was enough to deplete photogenerated carriers laterally in bulk c -GaN, fully eliminating the LA and TA signals simultaneously (not shown). Under the assumption that the initially sufficient hole density ($\sim 7 \times 10^{17}$ cm⁻³) was reduced below $0.1N_c$ under E_x , the ΔC_i^{stif} could be evaluated to be on the same order of the experimental results in Fig. 6(e), but with ~ 3 times smaller magnitudes. The question of this discrepancy between the experimental results and the analysis, which was not fully discussed in the current context, would be of particular importance in electrically controlling the elasticity and needs to be further investigated in structures with independent controllability of E_x and E_z .

V. ROLE OF LATERAL ELECTRIC FIELD IN DETECTION OF ACOUSTIC PHONON

In an optically isotropic medium such as c -GaN, dielectric tensor modulation due to shear strain can be detected only under oblique probe light incidence [37,41]. The shear strain in a laterally biased anisotropic medium, on the other hand, induces perturbation not only in the off-diagonal components, but also in the diagonal component of the dielectric tensor. Accordingly, the TA mode was optically detectable even when the incidence angle was normal to the surface, as represented by the digitized appearance in Figs. 4(a) and 5. In this section, we experimentally verify the optical anisotropy and corresponding changes in the detection sensitivity by measuring the acoustic modal properties as functions of different combinations in probe polarizations ϕ and incidence angles θ .

A. Electric-field-induced optical birefringence

Regarding the electrically manipulated crystal symmetry, E_x breaks the hexagonal symmetry of sample A via the application of the shear strain into monoclinic symmetry [33,57]. Concretely, the tilting of the principal axis away from the c

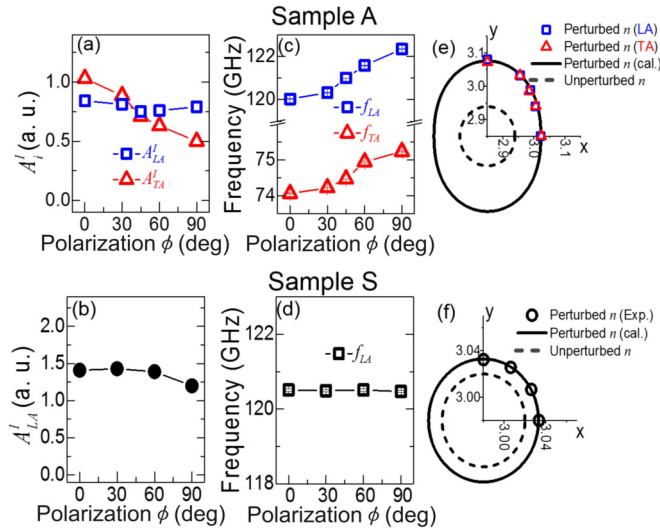


FIG. 7. Acoustic mode amplitudes of (a) sample A and (b) sample S for ϕ ranging from 0° to 90° in time domain I . Peak frequency for each acoustic mode in (c) sample A and (d) sample S as a function of ϕ . Refractive index ellipsoids for perturbed (at -5.5 V) and unperturbed (at 0 V) cases in (e) sample A and (f) sample S.

axis by E_x -induced monoclinic deformation could be revealed by angular perturbations of the elastic and dielectric tensors in the x - y plane.

Figures 7(a) and 7(b) show the spectral amplitudes of the dynamic Fabry-Perot oscillations from both samples at a V_{ext} value of -5.5 V, integrated over $\tau_i/2 < t < \tau_i$, as we rotate the probe polarization ϕ from the x axis at $\theta = 0^\circ$. In sample A, the TA amplitude (A_{TA}^I) monotonically decreased by about 50% with increasing ϕ , in clear contrast to the constant LA mode (A_{LA}^I) in Fig. 7(a), indicating that the TA mode was partially polarized along the same direction as E_x . Figure 7(b) shows that in sample S, A_{LA}^I was invariant with respect to ϕ , similarly with the behavior of the LA mode signal in sample A.

Despite the large value of V_{ext} , the modal frequencies f_{LA} and f_{TA} in sample A exhibited very similar increases with ϕ , as shown in Fig. 7(c), owing to the birefringence in the anisotropic region. In contrast, no notable change was observed for sample S, as shown in Fig. 7(d). As a function of ϕ , in this regard, the n value of sample A was extracted from either f_{LA} (blue squares) or f_{TA} (red triangles) in Fig. 7(e). The dashed inner circle in Fig. 7(e) displays the isotropic refractive index ellipsoid without E_x , whereas the solid outer circle exhibits the values calculated using the E_x -induced birefringence. In sample S under a symmetric potential distribution, the V_{ext} -induced birefringence and nonlinear elasticity was not observed in Fig. 7(f). The comparison of the samples therefore confirms the dominant role of the lateral potential gradient in manipulating the crystalline symmetry, concurrently with the modified optical coefficients.

B. Optical characterization of anisotropy in sample A

To further investigate the optical anisotropy in sample A, we varied the probe polarization ϕ at a fixed θ , now with an s -polarized analyzer in front of the probe detector. When the probe beam is incident on the sample at nonzero θ , the dynamic

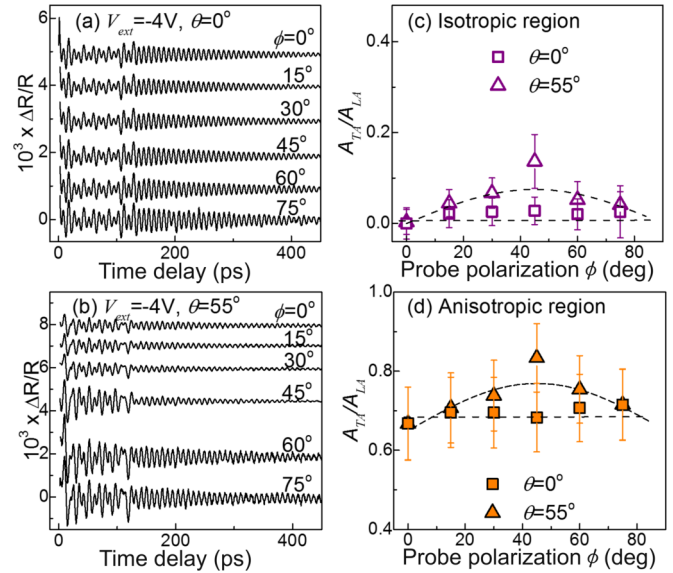


FIG. 8. Dynamic Fabry-Perot oscillations with variable probe polarization at (a) $\theta = 0^\circ$ and (b) $\theta = 55^\circ$ under -4 V. The ϕ -dependent relative amplitudes of the TA mode, $A_{\text{TA}}/A_{\text{LA}}$, in the (c) isotropic and (d) anisotropic regions at probe incidence angles of 0° and 55° .

Fabry-Perot interference for the TA mode is expected to be maximized at a ϕ value of 45° in such a geometry [32]. Since the pump-probe signals became attenuated as they propagated downward toward the n -GaIn side, the laser wavelength was further increased to 375 nm to ensure a deeper probe beam penetration depth ξ (~ 1.5 μm). The ϕ -dependent dynamic Fabry-Perot oscillations under -4 V are shown in Figs. 8(a) and 8(b) for normal and 55° probe incidence, respectively. To extract the spectral amplitudes of acoustic modes propagating in regions of different symmetry, we performed FFTs in two distinct temporal ranges, that is, in the anisotropic region for $t < \tau_{\text{LA}}$ (spatial extent: $0 < z < l_D + 440$ nm, where l_D is the n -depletion region width) and in the isotropic region for $t > \tau_{\text{TA}}$ ($z > l_D + 440$ nm). In Figs. 8(c) and 8(d), the relative amplitudes of the TA modes are traced with respect to ϕ in the isotropic and anisotropic regions, respectively.

As can be expected intuitively in the isotropic region, TA mode propagation was not detected under normal incident probe light, as shown in Fig. 8(c); in contrast, in the biased region, TA modes were observed consistently as ϕ changed, even for normal probe incidence in Fig. 8(d).

The different ϕ dependence of the modes is described in terms of the strain distributions along the z axis and the diagonal photoelastic coefficient for each mode. The result thus reveals that the diagonal components of the dielectric tensor were perturbed not only by the LA modes, but also by the TA modes [32,33]; both the LA and TA modes play roles in Maxwell's equation for normally incident light in Fig. 8(d).

When the probe beam is obliquely incident on the sample, the dynamic Fabry-Perot interference for a TA mode is thought to follow the change in $\Delta R/R \propto \sin(\phi) \cos(\phi)$, as denoted by the dashed line in Fig. 8(c) for an isotropic medium, because s -polarized light is flipped into p polarization upon reflection from the TA wave packets and vice versa for nonzero θ [37].

The isotropy of the unbiased region was confirmed by the agreement with the conventional $\sin(\phi)\cos(\phi)$ dependence, except for a hump at 45° . The deviation is attributed to the reduced sensitivity of the LA mode due to the screening effect of the TA mode, where the contribution of the diagonal dielectric tensor perturbation α is estimated to be about half the off-diagonal contribution β to the total amplitude of $\Delta R/R$ (see Appendixes A 2 and B). The result for the anisotropic region in Fig. 8(d), where the light reflection is now influenced by both the diagonal and off-diagonal perturbations of the TA modes, indicates that the off-diagonal effect of the TA waves on the probe polarization was boosted by the amount of anisotropy resulting in $A_{TA}/A_{LA} > 0.6$. In addition, the difference between A_{TA}/A_{LA} and the fitting curve at 45° in Fig. 8(d) was relatively small ($\sim 6\%$) since both the diagonal (α) and off-diagonal (β) contributions were mixed for $\Delta R/R$ of each acoustic mode.

C. External manipulation of the detection sensitivity in sample A

To gain a more quantitative insight into the relationship between F_i and the axial symmetry, we selectively measured the s -polarized component of the probe reflectance as a function of θ at -4 V, as shown in Fig. 9(a). The probe polarization angle ϕ was fixed at 45° to maximize the sensitivity of the x -polarized TA mode. As a result, more complicated phonon propagation dynamics appear in Fig. 9(a); the TA mode signals monotonically increased with θ not only in the purely anisotropic region (time domain I: $t < \tau_i$), but also in the purely isotropic region (time domain III: $2\tau_i < t < 3\tau_i$). We note that the abruptly suppressed TA mode at τ_{TA} was particularly prominent at $\theta = 0^\circ$ in Fig. 9(a). In contrast, the LA amplitude with θ varied in different time domains, slightly increasing up to τ_{LA} and then rapidly decreasing after $2\tau_{LA}$. In the intermediate region (time domain II: $\tau_i < t < 2\tau_i$), the increasing and decreasing tendencies were mixed for LA waves.

In order to experimentally quantify the θ -dependent acoustic modal amplitudes with different symmetries, a model for correlating the spatial dynamics in different symmetry regions with the time-domain signals was developed. The modal amplitudes A_i^j at f_i in the time domain $j = \{I, II, III\}$ were decomposed into ascending and descending parts, from

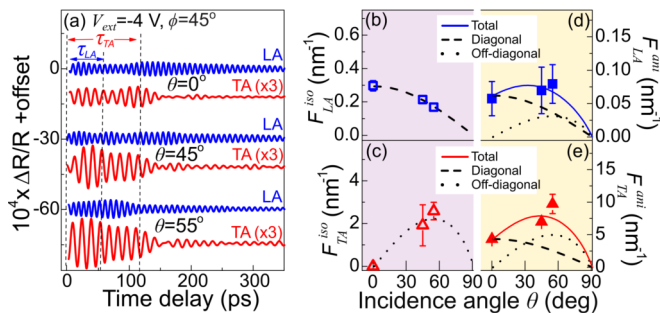


FIG. 9. (a) Time-domain signals from sample A for different probe incidence angles. Optical sensitivities of acoustic modes as a function of incident angle in the isotropic (b), (c) and anisotropic (d), (e) regions of sample A.

which the relative values of η_i^a , η_i^d , and the sensitivities in the anisotropic region, F_i^{ani} for $z \leq v_i \cdot \tau_i$, and isotropic region, F_i^{iso} for $z \geq v_i \cdot \tau_i$, could be extracted, as detailed in Appendix C. Accordingly, for different θ values, F_i^{ani} and F_i^{iso} were quantified as shown in Figs. 9(b) and 9(e).

The analytic expressions for F_i have been discussed separately for isotropic [37] and anisotropic crystals [28] in terms of the perturbations of the dielectric tensor due to strain. In isotropic materials, only the diagonal (off-diagonal) components in the perturbed dielectric tensor are induced by the LA (TA) waves. Subsequently, the opposite tendencies are predicted for F_{LA}^{iso} (dashed line) and F_{TA}^{iso} (dotted line) within our range of θ values, in agreement with the experimental values (empty squares and triangles) in Figs. 9(b) and 9(c).

On the other hand, to estimate F_i^{ani} , it is necessary to consider the mixed nature of the dielectric tensor modulations resulting from both diagonal and off-diagonal perturbations with empirically measured weighting factors to fit the experimental results in Figs. 9(d) and 9(e) as

$$\begin{pmatrix} F_{LA}^{\text{ani}} \\ F_{TA}^{\text{ani}} \end{pmatrix} = \begin{pmatrix} 0.22 & 0.014 \\ 14.6 & 2.25 \end{pmatrix} \begin{pmatrix} F_{LA}^{\text{iso}} \\ F_{TA}^{\text{iso}} \end{pmatrix}. \quad (5)$$

Indeed, the experimentally obtained values of F_i^{ani} in Figs. 9(d) and 9(e) were phenomenologically reproduced by linear combinations of the diagonal perturbations in the dielectric tensor ($\propto F_{LA}^{\text{iso}}$) and off-diagonal perturbations in the dielectric tensor ($\propto F_{TA}^{\text{iso}}$). Most importantly, the digitized appearance of the typically forbidden TA mode at $\theta = 0^\circ$ (Figs. 4 and 5) was verified by comparing the zero F_{TA}^{iso} [Fig. 9(c)] and nonzero value of F_{TA}^{ani} [Fig. 9(e)].

So far, the influence of E_x on the modal detection properties could be intuitively explained based on the symmetry-dependent dielectric tensor modulation $\Delta\epsilon$ by strains of a medium and/or acoustic modes. However, comparing the analytical expressions with the corresponding experimental results (see Appendix A 2), it was found that the coupling strength between $\Delta\epsilon$ and strains could not be relevantly quantified only with the existing method [28,32,37], photoelasticity, even with the nonlinearity parameters. This implies that other E_x -induced effects, such as the electro-optic effects, Franz-Keldysh effect, and carrier-density-dependent absorption change, should be incorporated into the photoelasticity-based model. Ignoring the contributions of the electro-optic and Franz-Keldysh effects due to the small intensity of E_x (< 1 kV/cm), the dielectric response by strains in sample A, where the hole density was assumed to be decreased by ~ 100 times via E_x -induced lateral transport, could be understood in a way that the symmetry-dependent characteristics of the dielectric tensor modulation were significantly intensified as the probe absorption was increased [58] with V_{ext} , similarly to the case of hole-depletion-induced abnormal elasticity in Sec. IV.

Although further detailed analyses are necessary to quantitatively investigate the vectorial influence of external fields on the anisotropic sensitivities, the results support the interpretation that the mixed contributions of both diagonal and off-diagonal modulations in the laterally biased region resulted in a gradual increment of F_{LA}^{ani} with increasing θ and allowed the TA mode detection, even at $\theta = 0^\circ$ (which was otherwise

forbidden [32,41]), demonstrating the electrical controllability of axial symmetry in piezoelectric diode structures.

VI. SUMMARY

In summary, we investigated the influence of the potential distribution on the properties of coherent acoustic phonons generated by ultrafast optical pulses. The crystal symmetry was broken by lateral electric fields in the structure with asymmetric potential gradients, which enabled optical activation and detection of the TA mode as well as modulating the frequencies of both the LA and TA modes. A series of detailed analyses of the propagation dynamics revealed abrupt suppression of the TA mode underneath the laterally biased depletion region, in striking contrast to the electrically independent appearance of the LA mode whose amplitude was described in terms of vertical electric fields. The results demonstrate the possibility of direct and active control of the modal acoustic phonons in semiconductors by electrically manipulating the crystal symmetry. These findings could provide a novel degree of freedom in engineering the lattice vibrations in crystalline heterostructures.

ACKNOWLEDGMENTS

We acknowledge useful discussions with Y. S. Lim and K. S. Kyhm. This work was funded by Samsung Electronics (Grant No. SRFC-IT1402-07).

APPENDIX A: ELASTIC AND PHOTOELASTIC TENSORS UNDER DIFFERENT SYMMETRIES

The elastic tensor C_{lm} of *c*-GaN can be perturbed by externally applied strains ε_3 (ε_{zz}) and ε_5 (ε_{zx}), as $C_{lm} = C_{lm}^0 + \Delta C_{lm} = C_{lm}^0 + C_{lmn}\varepsilon_n$, where C_{lm}^0 is the unperturbed elastic constant, and C_{lmn} is the TOE tensor [57]. Analogous results for the photoelasticity could be deduced based on the

geometric symmetry of the strained crystal [41,57] as $p_{lm} = p_{lm}^0 + \Delta p_{lm} = p_{lm}^0 + p_{lmn}\varepsilon_n$, where p_{lm}^0 is the unperturbed photoelastic constant, and p_{lmn} is the tensor components for the nonlinear photoelasticity. In Table I, the elastic and photoelastic tensors under different symmetry conditions are comparatively summarized.

1. Electrical modulation of modal velocity by elastic tensor perturbations

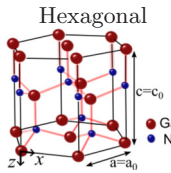
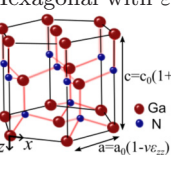
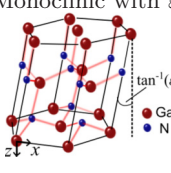
The acoustic velocities for LA and TA modes are obtained by solving the Christoffel equation [53] with the perturbed elastic constants and simplified under the assumption that (i) $C_{lm}^0 \gg \Delta C_{lm}$ and (ii) $C_{333}^M \sim C_{443}^M$:

$$v_{\text{LA}} = \frac{\sqrt{C_{33} + C_{44} + \sqrt{(C_{33} - C_{44})^2 + 4(C_{35})^2}}}{\sqrt{2\rho_0}} \approx \frac{\sqrt{C_{33} + \frac{(C_{35})^2}{C_{33} - C_{44}}}}{\sqrt{\rho_0}} \approx \frac{\sqrt{C_{33}^0 + C_{333}^H d_{33} E_z + \frac{(C_{355}^M)^2 d_{15}^2}{C_{33}^0 - C_{44}^0} E_z^2}}{\sqrt{\rho_0}} \quad (\text{A1})$$

and

$$v_{\text{TA}\parallel x} = \frac{\sqrt{C_{33} + C_{44} - \sqrt{(C_{33} - C_{44})^2 + 4(C_{35})^2}}}{\sqrt{2\rho_0}} \approx \frac{\sqrt{C_{44} - \frac{(C_{35})^2}{C_{33} - C_{44}}}}{\sqrt{\rho_0}} \approx \frac{\sqrt{C_{44}^0 + C_{443}^H d_{33} E_z - \frac{(C_{355}^M)^2 d_{15}^2}{C_{33}^0 - C_{44}^0} E_z^2}}{\sqrt{\rho_0}}. \quad (\text{A2})$$

TABLE I. Matrix representations of the elastic and photoelastic tensors with different symmetries.

Symmetry	Elastic tensor	Photoelastic tensor
 <p>Hexagonal</p>	$[C^0] = \begin{bmatrix} C_{11}^0 & C_{12}^0 & C_{13}^0 & 0 & 0 & 0 \\ C_{12}^0 & C_{11}^0 & C_{13}^0 & 0 & 0 & 0 \\ C_{13}^0 & C_{13}^0 & C_{33}^0 & 0 & 0 & 0 \\ 0 & 0 & 0 & C_{44}^0 & 0 & 0 \\ 0 & 0 & 0 & 0 & C_{44}^0 & 0 \\ 0 & 0 & 0 & 0 & 0 & C_{66}^0 \end{bmatrix}$	$[p^0] = \begin{bmatrix} p_{11}^0 & p_{12}^0 & p_{13}^0 & 0 & 0 & 0 \\ p_{12}^0 & p_{11}^0 & p_{13}^0 & 0 & 0 & 0 \\ p_{13}^0 & p_{13}^0 & p_{33}^0 & 0 & 0 & 0 \\ 0 & 0 & 0 & p_{44}^0 & 0 & 0 \\ 0 & 0 & 0 & 0 & p_{44}^0 & 0 \\ 0 & 0 & 0 & 0 & 0 & p_{66}^0 \end{bmatrix}$
 <p>Hexagonal with ε_{zz}</p>	$[C^0] + \begin{bmatrix} C_{113}^H & C_{123}^H & C_{133}^H & 0 & 0 & 0 \\ C_{123}^H & C_{113}^H & C_{133}^H & 0 & 0 & 0 \\ C_{133}^H & C_{133}^H & C_{333}^H & 0 & 0 & 0 \\ 0 & 0 & 0 & C_{443}^H & 0 & 0 \\ 0 & 0 & 0 & 0 & C_{443}^H & 0 \\ 0 & 0 & 0 & 0 & 0 & C_{663}^H \end{bmatrix} \varepsilon_{zz}$	$[p^0] + \begin{bmatrix} p_{113}^H & p_{123}^H & p_{133}^H & 0 & 0 & 0 \\ p_{123}^H & p_{113}^H & p_{133}^H & 0 & 0 & 0 \\ p_{133}^H & p_{133}^H & p_{333}^H & 0 & 0 & 0 \\ 0 & 0 & 0 & p_{443}^H & 0 & 0 \\ 0 & 0 & 0 & 0 & p_{443}^H & 0 \\ 0 & 0 & 0 & 0 & 0 & p_{663}^H \end{bmatrix} \varepsilon_{zz}$
 <p>Monoclinic with ε_{zx}</p>	$[C^0] + \begin{bmatrix} 0 & 0 & 0 & 0 & C_{155}^M & 0 \\ 0 & 0 & 0 & 0 & C_{255}^M & 0 \\ 0 & 0 & 0 & 0 & C_{355}^M & 0 \\ 0 & 0 & 0 & 0 & 0 & C_{465}^M \\ C_{155}^M & C_{255}^M & C_{355}^M & 0 & 0 & 0 \\ 0 & 0 & 0 & C_{465}^M & 0 & 0 \end{bmatrix} \varepsilon_{zx}$	$[p^0] + \begin{bmatrix} 0 & 0 & 0 & 0 & p_{155}^M & 0 \\ 0 & 0 & 0 & 0 & p_{255}^M & 0 \\ 0 & 0 & 0 & 0 & p_{355}^M & 0 \\ 0 & 0 & 0 & 0 & 0 & p_{465}^M \\ p_{155}^M & p_{255}^M & p_{355}^M & 0 & 0 & 0 \\ 0 & 0 & 0 & p_{465}^M & 0 & 0 \end{bmatrix} \varepsilon_{zx}$

2. Electrically controlled detection properties based on nonlinear photoelasticity

In the presence of lateral electric field, the refractive indices felt by the probe beam parallel to either the x axis ($n_{\mathcal{E}_x^{\text{ho}}}$) or the y axis ($n_{\mathcal{E}_y^{\text{ho}}}$) could be modeled based on nonlinear photoelasticity as

$$n_{\mathcal{E}_x^{\text{ho}}} \simeq \sqrt{\epsilon + p_{15}d_{15}E_x + d_{15}^2E_x^2(p_{15}p_{35} - p_{44}^2)/\epsilon} \quad (\text{A3})$$

and

$$n_{\mathcal{E}_y^{\text{ho}}} = \sqrt{\epsilon + p_{25}d_{15}E_x}. \quad (\text{A4})$$

The lateral field also affects the detection sensitivity F_i . When acoustic modes propagate in an isotropic medium along the z axis, LA strain waves η_3 and TA strain waves η_5 can locally modulate the dielectric tensor via the unperturbed photoelastic constants as

$$\Delta\epsilon = \begin{bmatrix} p_{13}^0\eta_3 \\ p_{13}^0\eta_3 \\ p_{33}^0\eta_3 \\ 0 \\ p_{44}^0\eta_5 \\ 0 \end{bmatrix} \equiv \begin{bmatrix} p_{13}^0\eta_3 & 0 & p_{44}^0\eta_5 \\ 0 & p_{13}^0\eta_3 & 0 \\ p_{44}^0\eta_5 & 0 & p_{33}^0\eta_3 \end{bmatrix}, \quad (\text{A5})$$

where the diagonal and off-diagonal components of $\Delta\epsilon$ are separated by η_3 and η_5 . Owing to the modally separated tensor components, different modal sensitivities depending on θ are expected [37,59] as $F_{\text{LA}}^{\text{iso}} \propto 4k'(1 - \epsilon^0)^{-1}p_{13}^0$ and $F_{\text{TA}}^{\text{iso}} \propto 2k_x k' k(k' - k'')^{-1}(\epsilon^0 k' k'' + k'^2)^{-1}p_{44}^0$, where $k = \omega_{\text{probe}}/c$, $k_x = k \sin(\theta)$, $k' = k \cos(\theta)$, and $k'' = \sqrt{\epsilon^0 k^2 - k_x^2}$. Conversely, the contribution of the diagonal (off-diagonal) components to $\Delta R/R$ can be represented as $F_{\text{LA}}^{\text{iso}}/p_{13}^0$ ($F_{\text{TA}}^{\text{iso}}/p_{44}^0$). This explains why TA modes in an isotropic material cannot be detected with normal probe incidence, at which $F_{\text{TA}}^{\text{iso}}$ becomes zero.

In contrast, in an anisotropic medium with E_x , the dielectric tensor is modulated by combinations of η_3 and η_5 via the perturbed photoelastic constants as

$$\Delta\epsilon = \begin{bmatrix} p_{13}\eta_3 + p_{15}\eta_5 \\ p_{13}\eta_3 + p_{25}\eta_5 \\ p_{33}\eta_3 + p_{35}\eta_5 \\ 0 \\ p_{35}\eta_3 + p_{44}\eta_5 \\ 0 \end{bmatrix} \equiv \begin{bmatrix} p_{13}\eta_3 + p_{15}\eta_5 & 0 & p_{35}\eta_3 + p_{44}\eta_5 \\ 0 & p_{13}\eta_3 + p_{25}\eta_5 & 0 \\ p_{35}\eta_3 + p_{44}\eta_5 & 0 & p_{33}\eta_3 + p_{35}\eta_5 \end{bmatrix}. \quad (\text{A6})$$

Accordingly, measurements of the modal propagation are influenced by both diagonal and off-diagonal perturbations as $F_{\text{LA}}^{\text{ani}} = \alpha(F_{\text{LA}}^{\text{iso}}/p_{13}^0)p_{13} + \beta(F_{\text{TA}}^{\text{iso}}/p_{44}^0)p_{35}$ and $F_{\text{TA}}^{\text{ani}} = \alpha(F_{\text{LA}}^{\text{iso}}/p_{13}^0)p_{15} + \beta(F_{\text{TA}}^{\text{iso}}/p_{44}^0)p_{44}$. α (β) is an empirical factor representing the mixed contribution of the diagonal (off-diagonal) perturbation in $\Delta\epsilon$ to the signal amplitude of mode i via, e.g., the modified LA (TA) sensitivity due to the interaction between TA (LA) waves and probe beams. The sensitivities in

the anisotropic region are now simplified in terms of those in the isotropic region as

$$\begin{pmatrix} F_{\text{LA}}^{\text{ani}} \\ F_{\text{TA}}^{\text{ani}} \end{pmatrix} = \begin{pmatrix} \alpha p_{13}/p_{13}^0 & \beta p_{35}/p_{44}^0 \\ \alpha p_{15}/p_{13}^0 & \beta p_{44}/p_{44}^0 \end{pmatrix} \begin{pmatrix} F_{\text{LA}}^{\text{iso}} \\ F_{\text{TA}}^{\text{iso}} \end{pmatrix}. \quad (\text{A7})$$

When the experimental results of the optical birefringence in Fig. 7(e) and the empirical weighting factors in Eq. (5) are compared with the corresponding coefficients from the photoelasticity-based models, the unperturbed photoelastic constants p_{lm}^0 were evaluated to be ~ 100 times larger than previously reported values [60] and the nonlinearity parameters p_{ijk}^H for E_z and p_{ijk}^M for E_x were estimated as $p_{155}^M \sim 7 \times 10^6 p_{13}^0$, $p_{133}^H \sim -4 \times 10^3 p_{13}^0$, $p_{355}^M \sim 1.4 \times 10^4 p_{44}^0$, and $p_{443}^H \sim 1.2 \times 10^4 p_{44}^0$. The order of the evaluated values implies that the photoelasticity-based approach is not enough to quantitatively describe the sizable changes in the dielectric constants; the influence of E_x -induced hole density variation should be incorporated, which was beyond the experimental scopes of current schemes.

APPENDIX B: ACOUSTIC SCREENING EFFECT ON MODAL SENSITIVITY

An acoustic wave packet locally perturbs the refractive index of a material, inducing modulations of the light reflection Δr and a corresponding transmission change $\Delta\Gamma = -\Delta r$, assuming that the phonon-induced absorption change is negligible. In most ultrasonic studies with a single acoustic mode, these modulations Δr and $\Delta\Gamma$ have been investigated independently using different pump-probe geometries for reflectivity and transmission. However, for measurements of more than one mode, the combined effect of the modulations on the detection sensitivity should be taken into account since the Δr ($\Delta\Gamma$) value of a mode can influence the $\Delta\Gamma$ (Δr) value of other modes.

Figure 10 shows the typical propagation of the strain pulses, the faster $\eta_{\text{LA}}(z,t)$ and the slower $\eta_{\text{TA}}(z,t)$, induced by the LA and TA modes in sample A, where the modal amplitudes are electrically controlled. The propagation of $\eta_{\text{TA}}(z,t)$, which lags behind $\eta_{\text{LA}}(z,t)$ because its propagation velocity is $\sim 50\%$ slower, can be simply traced by measuring the dynamic Fabry-Perot interference between the reflection from the surface r_0 and the reflection from $\eta_{\text{TA}}(z,t)$, Δr_{TA} [42]. However, the light reflection from $\eta_{\text{LA}}(z,t)$ is additionally modulated by a factor of $(\Delta\Gamma_{\text{TA}})^2$, as $\eta_{\text{TA}}(z,t)$ screens the probe beam incident on and reflected from $\eta_{\text{LA}}(z,t)$, which modifies the sensitivity F_{LA} and $\Delta R/R$ for the LA mode by the same amount.

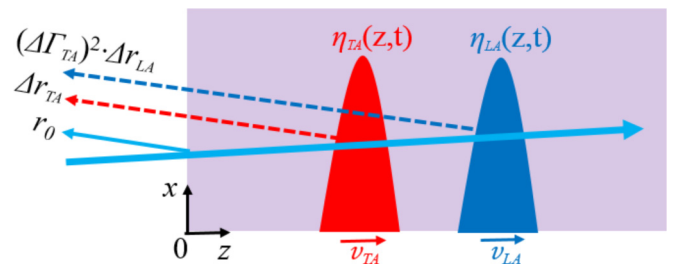


FIG. 10. Illustration of the $\Delta R/R$ measurement scheme for two different acoustic wave packets $\eta_{\text{LA}}(z,t)$ and $\eta_{\text{TA}}(z,t)$.

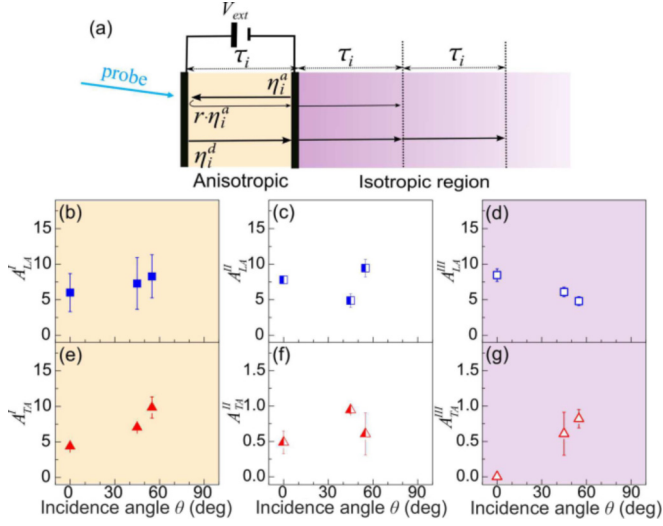


FIG. 11. (a) Propagation configurations of ascending (η_i^a) and descending (η_i^d) acoustic components in regions of different symmetry. (b)–(g) Fourier-transformed amplitudes of the dynamic Fabry-Perot oscillations for the LA (b)–(d) and TA (e)–(g) modes in the time domain $j = \{I, II, III\}$.

APPENDIX C: SENSITIVITY EXTRACTION METHOD

In Fig. 11, the Fourier-transformed amplitudes A_i^j of the signals in Fig. 9(a) were taken for mode index i in the time domains $j = \{I, II, III\}$. We assumed that the spatially concentrated acoustic strains are simplified to $\eta_i^a = \int_{D_i^a} \varepsilon_i(z) dz \delta(z + v_i t)$ for the ascending waves and $\eta_i^d = \int_{D_i^d} \varepsilon_i(z) dz \delta(z - v_i t)$ for the descending waves, where $\varepsilon_{LA}(z)$ [$\varepsilon_{TA}(z)$] corresponds to the normal (shear) strain, and the region of integration D_i^d (D_i^a) corresponds to the surface depletion region (the i region for the LA mode or the n -depletion region for the TA mode).

The ascending acoustic components η_i^a propagate toward the surface in time domain I , as described in Fig. 11(a); they then propagate back to the substrate after being reflected from the p -GaN/ITO interface during time domain II in the anisotropic region, and finally enter the isotropic region in time domain III . On the other hand, the descending components η_i^d , which were generated in the surface depletion region, traverse the anisotropic region in time domain I and propagate in the isotropic region toward the substrate when $t > \tau_i$. Therefore, A_i^j , which was experimentally extracted in Figs. 11(b)–11(g), could be analyzed as

$$\begin{aligned} A_i^I &= \kappa_i^I F_i^{\text{ani}} \eta_i^a + \kappa_i^I F_i^{\text{ani}} \eta_i^d \quad (0 < t < \tau_i), \\ A_i^{II} &= \kappa_i^I r F_i^{\text{ani}} \eta_i^a + \kappa_i^{II} F_i^{\text{iso}} \eta_i^d \quad (\tau_i < t < 2\tau_i), \\ A_i^{III} &= \kappa_i^{II} r F_i^{\text{iso}} \eta_i^a + \kappa_i^{III} F_i^{\text{iso}} \eta_i^d \quad (2\tau_i < t < 3\tau_i), \end{aligned} \quad (\text{C1})$$

where F_i^{ani} (F_i^{iso}) is the optical sensitivity of the acoustic (isotropic) region, and r is the phonon reflectivity at the p -GaN/ITO interface. $\kappa_i^j = \frac{\xi}{v_i \tau_i} (1 - e^{-\frac{v_i \tau_i}{\xi}}) e^{-(j-1)\frac{v_i \tau_i}{\xi}}$ is the probe light attenuation factor based on the wavelength dependent ξ , where $j = \{I, II, III\} \equiv \{1, 2, 3\}$. The sensitivity F_i^{ani} (F_i^{iso}) was expressed in terms of A_i^I (A_i^{III}) and then substituted into the right-hand side of the second equation in Eq. (C1) to determine the optimal values of $x = \eta_i^a / (\eta_i^a + \eta_i^d)$, which minimize the least-squares error $\delta(x)$ as

$$\delta(x) = |A_i^{II} - \kappa_i^I r \alpha_i x \eta_i - \kappa_i^{II} \beta_i (1-x) \eta_i|^2 \quad (0 < x < 1), \quad (\text{C2})$$

where $\eta_i = \eta_i^a + \eta_i^d$. On the basis of the least-squares fitting by Eq. (C2), x was evaluated to be ~ 0.7 (~ 0.6) for the LA (TA) mode, from which F_i^{ani} and F_i^{iso} could be experimentally extracted, as shown in Figs. 9(b)–9(e).

- [1] J.-K. Yu, S. Mitrovic, D. Tham, J. Varghese, and J. R. Heath, *Nat. Nanotechnol.* **5**, 718 (2010).
- [2] G. Pernot *et al.*, *Nat. Mater.* **9**, 491 (2010).
- [3] E. S. K. Young, A. V. Akimov, M. Henini, L. Eaves, and A. J. Kent, *Phys. Rev. Lett.* **108**, 226601 (2012).
- [4] I. S. Grudinin, H. Lee, O. Painter, and K. J. Vahala, *Phys. Rev. Lett.* **104**, 083901 (2010).
- [5] R. P. Beardsley, A. V. Akimov, M. Henini, and A. J. Kent, *Phys. Rev. Lett.* **104**, 085501 (2010).
- [6] A. Fainstein, N. D. Lanzillotti-Kimura, B. Jusserand, and B. Perrin, *Phys. Rev. Lett.* **110**, 037403 (2013).
- [7] I. Mahboob, K. Nishiguchi, A. Fujiwara, and H. Yamaguchi, *Phys. Rev. Lett.* **110**, 127202 (2013).
- [8] G.-W. Chern, C.-K. Sun, G. D. Sanders and C. J. Stanton, *Topics Appl. Phys.* **92**, 339 (2004).
- [9] C.-K. Sun, J.-C. Liang, C. J. Stanton, A. Abare, L. Coldren, and S. P. DenBaars, *Appl. Phys. Lett.* **75**, 1249 (1999).
- [10] H. Jeong, K. Min, S. Byun, C. J. Stanton, D. H. Reitze, J. K. Yoo, G. C. Yi, and Y. D. Jho, *Appl. Phys. Lett.* **100**, 092106 (2012).
- [11] C. Thomsen, H. T. Grahn, H. J. Maris, and J. Tauc, *Phys. Rev. B* **34**, 4129 (1986).
- [12] O. B. Wright and K. Kawashima, *Phys. Rev. Lett.* **69**, 1668 (1992).
- [13] J. S. Yahng, Y. D. Jho, K. J. Yee, E. Oh, J. C. Woo, D. S. Kim, G. D. Sanders, and C. J. Stanton, *Appl. Phys. Lett.* **80**, 4723 (2002).
- [14] C.-K. Sun, J.-C. Liang, and X.-Y. Yu, *Phys. Rev. Lett.* **84**, 179 (2000).
- [15] K. H. Lin, C. M. Lai, C. C. Pan, J. I. Chyi, J. W. Shi, S. Z. Sun, C. F. Chang, and C. K. Sun, *Nat. Nanotechnol.* **2**, 704 (2007).
- [16] M. R. Armstrong, E. J. Reed, K.-Y. Kim, J. H. Glowina, W. M. Howard, E. L. Piner, and J. C. Roberts, *Nat. Phys.* **5**, 285 (2009).
- [17] C. J. Stanton, G. D. Sanders, R. Liu, G.-W. Chern, C.-K. Sun, J. S. Yang, Y. D. Jho, J. Y. Sohn, E. Oh, and D. S. Kim, *Superlattices Microstruct.* **34**, 525 (2003).
- [18] C. S. Kim, J. H. Kim, H. Jeong, Y. D. Jho, H. K. Kwon, H. S. Lee, J. S. Park, K. Song, S. H. Kim, Y. J. Kim, D. Lee, and K. J. Yee, *Appl. Phys. Lett.* **100**, 101105 (2012).

- [19] C.-C. Chen, H.-M. Huang, T.-C. Lu, H.-C. Kuo, and C.-K. Sun, *Appl. Phys. Lett.* **100**, 201905 (2012).
- [20] Y.-C. Wen, T.-S. Ko, T.-C. Lu, H.-C. Kuo, J.-I. Chyi, and C.-K. Sun, *Phys. Rev. B* **80**, 195201 (2009).
- [21] D. H. Hurley, O. B. Wright, O. Matsuda, V. E. Gusev, and O. V. Kolosov, *Ultrasonics* **38**, 470 (2000).
- [22] M. E. Msall, O. B. Wright, and O. Matsuda, *J. Phys.: Conf. Ser.* **92**, 012026 (2007).
- [23] T. Pezeril, C. Klieber, S. Andrieu, and K. A. Nelson, *Phys. Rev. Lett.* **102**, 107402 (2009).
- [24] C. Klieber, T. Pezeril, S. Andrieu, and K. A. Nelson, *J. Appl. Phys.* **112**, 013502 (2012).
- [25] C. Klieber, T. Hecksher, T. Pezeril, D. H. Torchinsky, J. C. Dyre, and K. A. Nelson, *J. Chem. Phys.* **138**, 12A544 (2013).
- [26] K. A. Nelson, *J. Appl. Phys.* **53**, 6060 (1982).
- [27] K. A. Nelson and M. D. Fayer, *J. Chem. Phys.* **72**, 5202 (1980).
- [28] T. Pezeril, P. Ruello, S. Gougeon, N. Chigarev, D. Mounier, J.-M. Breteau, P. Picart, and V. Gusev, *Phys. Rev. B* **75**, 174307 (2007).
- [29] M. Lejman, G. Vaudel, I. C. Infante, P. Gemeiner, V. E. Gusev, B. Dkhil, and P. Ruello, *Nat. Commun.* **5**, 4301 (2014).
- [30] P. Walker, R. P. Champion, A. J. Kent, D. Lehmann, and Cz. Jasiukiewicz, *Phys. Rev. B* **78**, 233307 (2008).
- [31] T. Pezeril, V. Gusev, D. Mounier, N. Chigarev, and P. Ruello, *J. Phys. D: Appl. Phys.* **38**, 1421 (2005).
- [32] O. Matsuda, O. B. Wright, D. H. Hurley, V. E. Gusev, and K. Shimizu, *Phys. Rev. Lett.* **93**, 095501 (2004).
- [33] H. Jeong, Y. D. Jho, and C. J. Stanton, *Phys. Rev. Lett.* **114**, 043603 (2015).
- [34] C. Rossignol, J. M. Rampnoux, M. Perton, B. Audoin, and S. Dilhaire, *Phys. Rev. Lett.* **94**, 166106 (2005).
- [35] T. Dehoux, N. Chigarev, C. Rossignol, and B. Audoin, *Phys. Rev. B* **76**, 024311 (2007).
- [36] T. Pezeril, N. Chigarev, P. Ruello, S. Gougeon, D. Mounier, J.-M. Breteau, P. Picart, and V. Gusev, *Phys. Rev. B* **73**, 132301 (2006).
- [37] O. Matsuda and O. B. Wright, *Anal. Sci.* **17**, S216 (2001).
- [38] Y. D. Jho, J. S. Yahng, E. Oh, and D. S. Kim, *Appl. Phys. Lett.* **79**, 1130 (2001).
- [39] Y. D. Jho, J. S. Yahng, E. Oh, and D. S. Kim, *Phys. Rev. B* **66**, 035334 (2002).
- [40] I. L. Guy, S. Muensit, and E. M. Goldys, *Appl. Phys. Lett.* **75**, 4133 (1999).
- [41] J. F. Nye, *Physical Properties of Crystals* (Oxford University Press, Oxford, 1957).
- [42] R. Liu, G. D. Sanders, C. J. Stanton, C. S. Kim, J. S. Yahng, Y. D. Jho, K. J. Yee, E. Oh, and D. S. Kim, *Phys. Rev. B* **72**, 195335 (2005).
- [43] M. Yamaguchi, T. Yagiz, T. Azuhatax, T. Sotax, K. Suzukix, S. Chichibuk, and S. Nakamura, *J. Phys.: Condens. Matter* **9**, 241 (1997).
- [44] C.-T. Yu, K.-H. Lin, C.-L. Hsieh, C.-C. Pan, J.-I. Chyi, and C.-K. Sun, *Appl. Phys. Lett.* **87**, 093114 (2005).
- [45] U. Jahn, S. Dhar, M. Ramsteiner, and K. Fujiwara, *Phys. Rev. B* **69**, 115323 (2004).
- [46] A. S. Barker, Jr. and M. Ilegems, *Phys. Rev. B* **7**, 743 (1973).
- [47] M. Wraback, H. Shen, J. C. Carrano, T. Li, J. C. Campbell, M. J. Schurman, and I. T. Ferguson, *Appl. Phys. Lett.* **76**, 1155 (2000).
- [48] K.-H. Lin, G.-W. Chern, S.-W. Chu, C.-K. Sun, H. Xing, Y. Smorchkova, S. Keller, U. Mishra, and S. P. DenBaars, *Appl. Phys. Lett.* **81**, 3975 (2002).
- [49] M. Foussekis, A. A. Baski, and M. A. Reshchikov, *Appl. Phys. Lett.* **94**, 162116 (2009).
- [50] A. Polian, M. Grimsditch, and I. Grzegory, *J. Appl. Phys.* **79**, 3343 (1996).
- [51] T. Wittkowski, J. Jorzick, H. Seitz, B. Schröder, K. Jung, and B. Hillebrands, *Thin Solid Films* **398–399**, 465 (2001).
- [52] *Sensing with Terahertz Radiation*, edited by D. Mittleman (Springer, Berlin, 2003).
- [53] See, e.g., J. F. Rosenbaum, *Bulk Acoustic Wave Theory and Devices* (Artech House, Norwood, 1988).
- [54] A. R. Hutson and D. L. White, *J. Appl. Phys.* **33**, 40 (1962).
- [55] M. Kobayashi, K. Takesawa, and I. Yokota, *Phys. Status Solidi A* **47**, 657 (1978).
- [56] A. D. Bykhovski, B. L. Gelmont, and M. S. Shur, *J. Appl. Phys.* **81**, 6332 (1997).
- [57] R. F. Fuck and I. Tsvankin, *Geophysics* **74**, WB79 (2009).
- [58] B. R. Bennett, R. A. Soref, and J. A. D. Alamo, *IEEE J. Quantum Electron.* **26**, 113 (1990).
- [59] O. Matsuda and O. B. Wright, *Rev. Sci. Instrum.* **74**, 895 (2003).
- [60] S. Y. Davydov, *Semiconductors* **36**, 41 (2002).